PCCP

ROYAL SOCIETY OF CHEMISTRY

PAPER

View Article Online
View Journal | View Issue

Check for updates

Cite this: *Phys. Chem. Chem. Phys.*, 2025, **27**, 10331

Balancing fracture toughness and ionic conductivity in lithium thiosilicate glassy electrolytes†

Søren S. Sørensen,[a] Daniel Boysen,‡[a] Esben R. Lindbjerg,‡[a] Helle N. Mortensen,‡[a] Kaja T. Lippert,‡[a] Sisse M. Diget,‡[a] Zuzanna Konieczna,‡[a] Matthieu Micoulaut[b] and Morten M. Smedskjaer *[a]

Received 21st January 2025,
Accepted 17th April 2025

DOI: 10.1039/d5cp00285k

rsc.li/pccp

The use of solid instead of liquid electrolytes can lead to increased battery capacity and safety. However, solid-state electrolytes bring a number of challenges, especially the lower ionic conductivity and the risk of material cracking, ultimately causing battery failure. This work addresses these challenges by probing the archetypical electrolyte family of lithium thiosilicate glasses (xLi$_2$S–(100−x)SiS$_2$) to study the influence of lithium sulfide content on the mechanical and ionic transport properties. Interestingly, we find a decreasing fracture toughness and increasing ionic conductivity with increasing Li$_2$S content. We ascribe this to the depolymerization of the glassy network with increasing Li$_2$S content and a decoupled activation mechanism of thermal diffusion and movement under mechanical strain. Ultimately, the investigated glasses offer insights into battery operation where the electrolyte is continuously cycled through high- and low-lithium content states. In turn, this highlights the need to consider the material properties across a wide range of compositions when engineering future solid-state electrolytes.

1. Introduction

Lithium-ion batteries constitute the majority of transportable batteries in, *e.g.*, cell phones and electric cars,[1,2] due to their high energy densities, availability, and generally long lifetime.[3] However, the currently used cell design relies on liquid electrolytes, in some cases posing risks due to battery leaks and failure.[3] In comparison, solid-state batteries offer compelling improvements, such as higher energy density and improved resistance to fires and explosions compared to liquid electrolytes.[4,5] As electrodes (cathode, anode) are generally already solids, the emergence of solid-state electrolytes (SSEs) is the major obstacle against the development of an all-solid battery.

Multiple systems have been proposed as solid electrolyte candidates. Oxide-based lithium silicon, phosphate, and germanate glasses and ceramics have shown relatively high ionic conductivities approaching $\sim 10^{-4}$ S cm^{-1} at room temperature while being stable in an ambient atmosphere.[4–7] Sulfide-based electrolytes show even higher ionic conductivity at room temperature (*e.g.*, $\sim 10^{-2}$ S cm^{-1} for a Li$_{10}$GeP$_2$S$_{12}$ system) approaching that of liquid electrolytes ($\sim 10^{-2}$ S cm^{-1}).[4,6–8] In addition to ionic conductivity, the mechanical properties of SSEs also need to be considered. This is because cracking can occur due to the repeated cycling of lithium ions through the SSE, causing repetitive stress, possible material fracture, and ultimately short circuiting of the battery.[5,9,10] Despite this shortcoming, atomic-scale understanding of the mechanical and fracture-related properties and their relation to the ionic conductivity of SSEs is still lacking. This is likely due to the significant challenge in accessing these parameters in inert environments and in environments mimicking battery operation.

Among the SSEs with high ionic conductivity is the family of alkali thiosilicate glasses, with lithium thiosilicates (xLi$_2$S–(100−x)SiS$_2$) having the highest ionic conductivity of about 10^{-3} S cm^{-1}.[6,11–13] Lithium thiosilicate glasses have been experimentally produced in the compositional range of x = {40–60} with the 50Li$_2$S–50SiS$_2$ composition being the most commonly studied. While the sulfide-based electrolytes feature higher ionic conductivities than the oxide counterparts, both their elastic moduli and yield strengths are generally lower than oxides (typically by a factor of 2–3) as caused by the lower strength of the Si–S compared to the Si–O bond.[14–16] To our knowledge, no experimental probing of the fracture behavior of

---

[a] *Department of Chemistry and Bioscience, Aalborg University, DK-9220 Aalborg, Denmark. E-mail: mos@bio.aau.dk*

[b] *Laboratoire de Physique Théorique de la Matière Condensée, Sorbonne Université, CNRS UMR 7600, 4 Place Jussieu, 75252 Paris Cedex 05, France*

† Electronic supplementary information (ESI) available. See DOI: **https://doi.org/10.1039/d5cp00285k**

‡ These authors contributed equally.

lithium thiosilicate glasses exists, but the fracture toughness of $Li_2S–P_2S_5$ glass has been found to be in the range of 0.2–0.3 MPa $m^{0.5}$,[17] *i.e.*, lower than the typical value of oxide glasses (0.5–1.0 MPa $m^{0.5}$).[18] While the lithium thiosilicate system is in fact a rather well-studied glassy electrolyte with measurements of both thermodynamics, structure, and ionic character, simulation-based studies are highly scarce due to the lack of available (or reliable) force fields with a few exceptions focusing on sodium thiosilicates.[19,20] However recently, a classical force field was developed specifically for the lithium thiosilicate system[21] based on the fitting of a Buckingham potential form to a number of crystalline lithium thiosilicate structures. This has opened opportunities for studying the atomic scale ion dynamics and fracture of this glass family, since the cost of *ab initio* molecular dynamics prohibit studies of especially fracture behavior.

Using the recently developed force field by Poitras and Micoulaut[21] for molecular dynamics (MD) simulations and building upon previous studies of equilibrium mechanics and diffusion in selected thiosilicates,[22,23] we here study a wider series of lithium thiosilicate ($x Li_2S–(100-x)SiS_2$) glasses with $x = \{30, 40, 50, 60\}$. By probing their structure, dynamics, and finally fracture mechanics, we identify relations between ionic and fracture behavior. These features are important since it is known that battery charging/discharging induces volumetric changes in the cathode and anode materials, which in turn introduce strain and mechanical deformation at the interface with the solid electrolyte.[24,25] It is, therefore, important to infer how structure driven by compositional changes impacts specific mechanical and fracture behavior, something often not considered in the existing literature.[26] Here, we identify a negative relation between ionic conductivity and fracture toughness, highlighting the complex interplay between performance and stability in glassy SSEs.

2. Methods

2.1 Simulation details

All simulations were performed in the LAMMPS software package using the recently developed pair potential for lithium thiosilicate glasses. This potential employs a Buckingham-potential form,[21]

$$U_{ij}(r_{ij}) = A_{ij}e^{-r/\rho_{ij}} + \frac{q_i q_j}{r_{ij}} - \frac{C_{ij}}{r_{ij}^6}, \qquad (1)$$

where U denotes potential energy, A_{ij}, ρ_{ij}, and C_{ij} are constants unique for atomic type pairs, ij, r is the separation of two atoms with index i and j, while q is the atomic charge. The specifically used force field parameters are given in Table 1. The cutoff of short-range interactions was set to 8.0 Å, while long-range Coulombic interactions were treated using the PPPM algorithm (practically with a shift from real- to inverse space calculations at 12 Å) at an accuracy of 10^{-5}. The timestep was always 1 fs.

2.2 Glass preparation

Random structures were generated for $x Li_2S–(100-x)SiS_2$ glasses with $x = \{30, 40, 50, 60\}$ with a total of 3000 atoms while avoiding atoms within a separation of 1.4 Å. Simulation box sizes were fixed according to experimental densities of the glasses[13,27] as shown in Table 2. Initial structures were then structurally minimized before initiating dynamics. Dynamics were initiated at 300 K for 10 ps to relax the structure before heating to 2000 K over the course of 100 ps. Afterwards, the structures were mixed at 2000 K for 100 ps and then cooled to 300 K at a rate of 1 K ps^{-1} before finally relaxing for another 100 ps at 300 K. All steps were performed in the NVT ensemble using a Nosé–Hoover thermostat.[28,29]

Table 1 Employed force field parameters for the present simulations of $x Li_2S–(100 - x)SiS_2$ glasses. The force field parameters were taken from ref. 21

Atom i (−)	Atom j (−)	A_{ij} (kJ mol^{-1})	ρ_{ij} (Å)	C_{ij} (kJ mol^{-1} $Å^{-6}$)
$Si^{+2.4}$	$Si^{+2.4}$	200 678 290.92765	0.072	0
$Si^{+2.4}$	$S^{-1.2}$	7 718 820.0	0.178	0
$Si^{+2.4}$	$Li^{+0.6}$	528 220 069.276	0.076	0
$S^{-1.2}$	$S^{-1.2}$	10 613 383.8	0.284	96 485.0
$S^{-1.2}$	$Li^{+0.6}$	9 648 530.75	0.182	0
$Li^{+0.6}$	$Li^{+0.6}$	677 340 912.466	0.080	0

2.3 Scattering properties

To compute the scattering functions of the probed glasses, we first recorded the partial pair distribution functions of all atomic pairs in the material [$g_{ij}(r)$]. The X-ray and neutron structure factor of the simulated structures were computed by first calculating the partial structure factors [$S_{ij}(Q)$] as,[30]

$$S_{ij}(Q) = 1 + \rho_a \int_0^{r_{\max}} 4\pi r^2 (g_{ij}(r) - 1) \frac{\sin(Qr)}{Qr} \frac{\sin\left(\frac{\pi r}{r_{\max}}\right)}{\frac{\pi r}{r_{\max}}} dr, \qquad (2)$$

where Q is the wave vector, ρ_a is the average atom number density, $r_{\max}$ is the maximum radius for the integration (half box size). Finally, the $\sin(\pi r/r_{\max})/(\pi r/r_{\max})$ term is a Lorch type function used to reduce ripples of the Fourier transform due to the finite cutoff of r where $r_{\max}$ is the maximum separation recorded in the $g(r)$. The total neutron structure factor was then calculated from the partial structure factors as,

$$S_N(Q) = \left(\sum_{i,j=1}^{n} c_i c_j b_i b_j\right)^{-1} \sum_{i,j=1}^{n} c_i c_j b_i b_j S_{ij}(Q). \qquad (3)$$

where c_i and b_i are concentration and scattering length, respectively. For estimating neutron spectra, neutron coherence lengths of −2.220, 2.847, and 4.149 were used for ^{7}Li, ^{Nat}Si, and ^{Nat}S, respectively. Following the same procedure, we used

Table 2 Experimental densities for the studied glasses as obtained experimentally in ref. 13 and 27 and the corresponding box side length for the present simulations using 3000 atoms

x in $x Li_2S–(100 - x)SiS_2$	30	40	50	60
Density (g cm^{-3})	2.29	2.01	1.89	1.81
Box side length (Å)	38.44	39.33	39.31	38.94

the number of electrons in each element as the weight in the calculations of the X-ray structure factors (Li: 3, Si: 14, S: 16).

2.4 Elastic properties

Elastic constants were estimated by deforming the produced glass simulation boxes: first, the *xx*-direction was elongated in 70 steps, with each step consisting of 0.05% deformation of the initial simulation box size, while the stress was recorded to yield the C_{11} elastic constant. Next, the *xy*-plane was deformed in a shear strain in 70 steps of 0.1 Å, practically deforming the simulation box away from a cubic and into a monoclinic shape. Next, by recording the shear stress on the displaced plane, we evaluated the C_{44} elastic constant through linear regression of the shear strain *vs.* shear stress curve. Then, the last elastic constant C_{12} (in the assumption of an isotropic material) as well as the elastic moduli (Young's modulus E, shear modulus G, bulk modulus B, and Poisson's ratio ν) were calculated as,

$$C_{12} = C_{11} - 2C_{44}, \tag{4}$$

$$E = \frac{(C_{11} - C_{12})(C_{11} + 2C_{12})}{C_{11} + C_{12}}, \tag{5}$$

$$G = C_{44}, \tag{6}$$

$$B = \frac{C_{11} + 2C_{12}}{3}, \tag{7}$$

$$\nu = \frac{C_{12}}{C_{11} + C_{12}}. \tag{8}$$

Finally, we note that we computed the stress (both for the estimation of the elastic properties and when used in the fracture simulations) following the standard method for computing pressure in LAMMPS. Specifically, a stress tensor for directions I and J (where I and J can take directions x, y, z) was computed as,

$$P_{IJ} = \frac{1}{V}\sum_{k=1}^{N} m_k v_{k_I} v_{k_J} + \frac{1}{V}\sum_{k=1}^{N} r_{k_I} f_{k_J}$$

where m, v, r, and f are mass, velocity, position, and force of/on atom k in the given direction (I or J), respectively. This tensor was used directly to assess the total stress in each direction during simulations.

2.5 Fracture toughness

To estimate the fracture toughness (K_{Ic}) of the studied glasses, we followed the approach by Brochard.[31] In detail, we expanded the initially obtained glass structures into replications of 1 × 3 × 2. This yielded a total of 18 000 atoms, which is similar in size to that of related studies.[32–34] Then, an elliptic shape was cut out from the middle of the sample box with a width of 5/24 of the simulation box and a height of 1/5 of the crack width (*i.e.*, 1/24 of the box width). Next, these configurations were relaxed for 1 ns in the NVT ensemble at 300 K followed by a structural minimization to relax the precrack. Finally, an elongation was performed in 110 steps each of 1% strain in the *zz*-direction in which all samples experienced full cracking. After each incremental elongation step, the sample was minimized and subsequently relaxed in the NVT ensemble for 10 ps corresponding to a strain rate of 10^{-3} ps^{-1}. The stress was simultaneously recorded in the *zz*-direction (σ_z) to yield the so-called critical energy release rate (G_{c}),

$$G_{\mathrm{C}} = \frac{L_x L_y}{\Delta A_{\infty}} \int_{L_{z,0}}^{L_{z,\max}} \sigma_z \mathrm{d}L_z, \tag{9}$$

where L is the length of the specified direction and ΔA_{∞} is created crack surface area during fracture (as obtained using the surface area estimation implemented in OVITO[35]). In addition to the strain rate of 10^{-3} ps^{-1}, we tested a strain rate of 10^{-4} ps^{-1} (Fig. S1, ESI†), finding only a minor effect on the obtained stress–strain response and no significant difference in the overall characteristics (tailing, area under curve, *etc.*). Now, by assuming the fracture surface energy $\gamma = G_{\mathrm{C}}/2$, K_{Ic} was estimated by the Irwin formula,

$$K_{\mathrm{Ic}} = \sqrt{\frac{2\gamma E}{1 - \nu^2}}, \tag{10}$$

where the Young's modulus and Poisson's ratio from the simulations were used.

2.6 Ionic conductivity

To estimate the ionic conductivity, we first computed the mean-square displacement (MSD) as,

$$\mathrm{MSD}_i(t) = \langle r_i^2(t) \rangle = \left\langle \frac{1}{N_i}\sum_{j=1}^{N_i} \left|\mathbf{r}_j(t) - \mathbf{r}_j(0)\right|^2 \right\rangle, \tag{11}$$

where t is time, i denotes an atomic type, N_i is the total number of i atoms, and $\mathbf{r}$ is the atomic coordinate. The self-diffusion coefficient (D_i) is given by slope of the MSD at high t, that is, in the diffusive regime. Given that this regime has been achieved, D_i is given by,

$$D_i = \frac{1}{6}\lim_{t\to\infty} \frac{\langle r_i^2(t) \rangle}{\mathrm{d}t}. \tag{12}$$

Now, under the assumption that cross correlations are negligible (*e.g.*, see discussion in ref. 20), the ionic conductivity (σ_i) of a system at a given temperature (T) is given by the Nernst–Einstein equation,

$$\sigma(T) = \sum_i \frac{N_i Z_i^2 e^2}{V k_{\mathrm{B}} T} D_i, \tag{13}$$

where Z_i is the charge of species i, e is the elementary charge, V is simulation box volume, and k_{B} is the Boltzmann constant.

3. Results and discussion

3.1 Structure

The four glasses with compositions x = {30, 40, 50, 60} in the xLi$_2$S–(100−x)SiS$_2$ glass family were prepared in the NVT ensemble to ensure that the final structures follow the densities reported in the literature.[27] While the employed force field

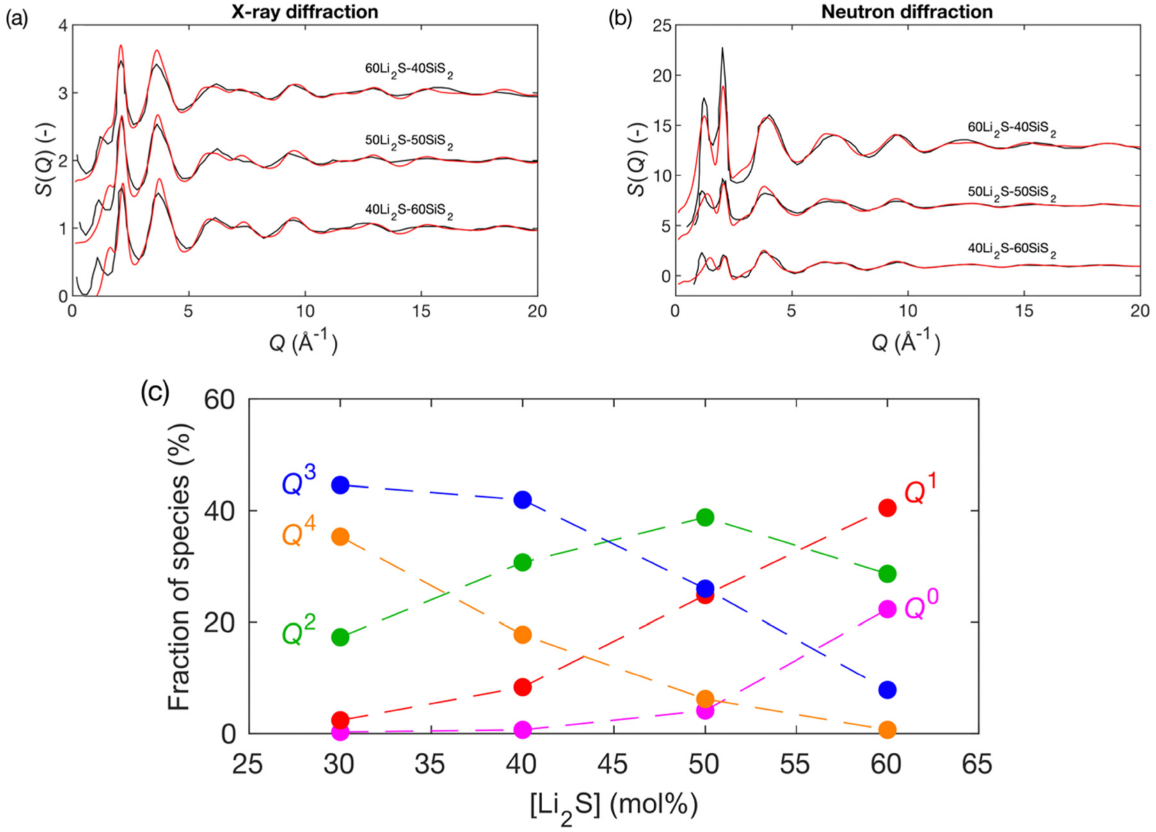

Fig. 1 Structure factors [$S(Q)$] from (a) X-ray and (b) neutron diffraction experiments, where simulation results (red) are compared to experimental data (black) from ref. 27 for the x = {40, 50, 60} glasses in the $x\mathrm{Li_2S}$–(100−x)$\mathrm{SiS_2}$ series. Generally, a high level of structural agreement is found between the simulated and experimental data. Spectra in both panels (a) and (b) are shifted vertically in steps of +1 for clarity. (c) Simulated composition dependence of Q^n speciation for all studied $x\mathrm{Li_2S}$–(100 − x)$\mathrm{SiS_2}$ glasses. The dashed lines in panel (c) serve as guides for the eye.

parameters[21] were parameterized to replicate two $\mathrm{Li_2S}$–$\mathrm{SiS_2}$ crystalline structures, in the present work we have used the force field in an extended composition range. To verify that we obtain realistic glass structures, we compare the X-ray and neutron structure factors of the computed glasses to experimental measurements (from ref. 27) in Fig. 1a and b. We find overall good structural agreement between simulations and experiments for both X-ray (Fig. 1a) and neutron (Fig. 1b), especially at Q-values above 2 Å^{-1} while the peak at the lowest Q-values in the $S(Q)$ (the so-called first sharp diffraction peak, FSDP) is rather poorly predicted, although it is present. This agreement at high Q suggests that the short-range structure is well-described for the glasses, whereas the medium-range order likely features some deviations compared to experimental glasses as recently discussed.[36] This seems to be especially pronounced for the glasses with lowest $\mathrm{Li_2S}$ content in the case of both X-ray and neutron structure factors, and these do not have a special interest for fast-ion applications.

We next investigate the structural depolymerization of the sulfide glass network with increasing $\mathrm{Li_2S}$ content. While no experimental data exist for validation of the simulation results, it is generally believed that sulfide glasses tend to share the same method of ''modification'' as the oxide glasses, *i.e.*, upon modifier addition (*e.g.* $\mathrm{Li_2S}$, or more generally alkali, alkaline earth, or transition metal sulfides and/or oxides), bridging sulfurs will be partially replaced with non-bridging sulfurs, effectively breaking up the network (see schematic in Fig. S2, ESI†) and commonly lowering, *e.g.*, mechanical moduli and glass transitions temperatures.[13,37,38] Structurally this is described by the so-called Q^n-distribution, where n is the number (0–4) of bridging sulfur atoms around each network cation (in this work Si). We note that the Q^n-distribution is normalized by the amount of Si-atoms, *i.e.*, the summed fraction of Q^n species is by definition 100% (that is, $f(Q^0) + f(Q^1) + f(Q^2) + f(Q^3) + f(Q^4) = 100\%$). The computed Q^n distribution for the studied glasses is shown in Fig. 1c, revealing an overall network depolymerization with increasing amount of $\mathrm{Li_2S}$, *i.e.* the average n reduces with increasing x. This agrees with the expectation, *i.e.*, the glasses change from being highly polymerized for x = 30 and dominated by Q^3 and Q^4 units to a very depolymerized structure dominated by Q^0, Q^1, and Q^2 units for x = 60.

3.2 Mechanical properties

Next, we evaluate the mechanical properties of the glasses by performing forced longitudinal and shear stretching to compute the C_{11} and C_{44} elastic constants (see Methods), which are then used to calculate the Young's, shear, and bulk moduli

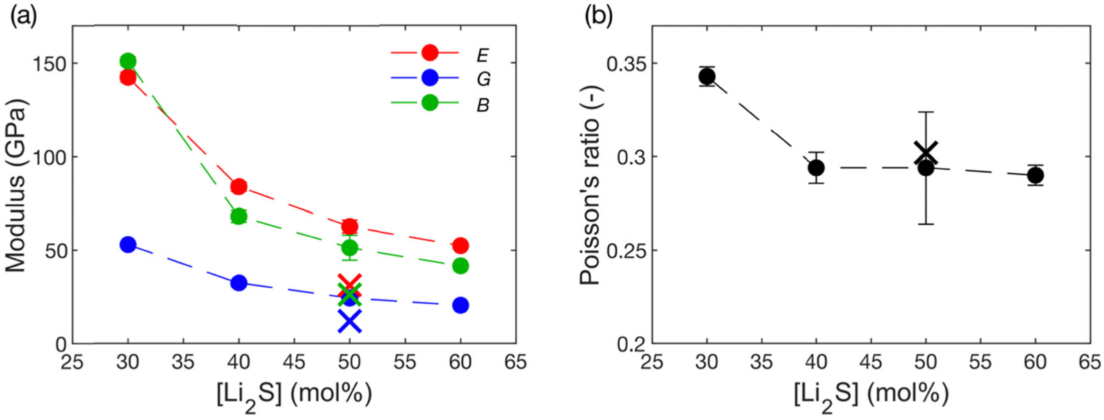

Fig. 2 (a) Young's, bulk, and shear moduli (*E*, *B*, *G*) and (b) Poisson's ratio (*ν*) as a function of Li_2S content in the studied $x$$Li_2S$–(100−$x$)$SiS_2$ glasses. The circular data points represent the results from the present simulations, while the crosses represent experimental values from Kato *et al.*[16] determined using a compressed pellet of 50Li_2S–50SiS_2 glass. The dashed lines serve as guides for the eye.

(*E*, *G*, *B*, respectively) as well as the Poisson's ratio (*ν*). As shown in Fig. 2a, the elastic moduli decrease with increasing Li_2S content. That is, *E* and *B* decrease from ∼140 to ∼50 GPa, while *G* decreases from ∼50 to ∼20 GPa when the Li_2S content increases from 30 to 60 mol%. To our knowledge, the elastic properties of these glasses have not been determined experimentally, except in the case of the 50Li_2S–50SiS_2 glass. Using a pelletized sample, the following results were obtained: E = 31.0 GPa, B = 26.1 GPa, G = 11.9 GPa, and ν = 0.302.[16] In the present simulations, we find a value of *E* for 50Li_2S–50SiS_2 glass to be ∼60 GPa, suggesting that the simulated elastic moduli herein are overestimated, likely by a factor of ∼2. This overestimation may arise because the potential was parameterized to reproduce structure and not mechanical properties. However, the observed qualitative trend of decreasing moduli with Li_2S content is expected from the network depolymerization (Fig. 1c), as in the archetypical alkali silicates,[39] effectively lowering the network rigidity, making deformation easier. In addition to the moduli, Poisson's ratio also monotonically decreases, from around 0.34 to 0.29 when the fraction of Li_2S increases from 30 to 40 mol% and then a smaller decrease of *ν* for compositions with higher fraction of Li_2S. To our knowledge, no experimental data of *ν* exist for beyond the experimental value shown as a cross in Fig. 2b. As such, these results might be regarded as benchmark values for upcoming experimental or theoretical studies. We also note how previous works have linked increasing depolymerization with increasing Poisson's ratio for *e.g.* oxide network glasses,[40] but that this relation does not seem to be strictly transferable to the sulfides.

In addition to the equilibrium mechanics, one of the main drawbacks of SSEs is their propensity for cracking, effectively decreasing battery performance or even full malfunction. Here, we study the nature of fracture in the range of studied lithium thiosilicate glassy electrolytes. To this end, we start from the simulation cells formed from the described quenching procedure (see Methods). From a macroscopic point of view, microscopic (non-visible) cracks are ultimately responsible for the practical strength of brittle materials, including inorganic glasses. We mimic this effect by introducing a pre-crack to a replicated (1 × 3 × 2) simulation cell of each glass composition to guide the crack opening. This is done by forcing the pre-crack to expand by elongation (in steps of 1%) of the simulation box to 140% of its initial size while simultaneously recording the stress in the direction of elongation. This effect of stretching mimics, to some extent, the volume changes associated with charging/discharging processes as caused by the inhomogeneous distribution of lithium ions in the electrolyte during battery cell operation. However, the simulations do not directly take this migration of lithium ions into account. Rather, our simulations provide the bulk fracture-properties of the electrolyte materials and as such, an estimation of their local mechanical performance in the electrolyte. The elongation process is illustrated in Fig. 3a, while the resulting stress–strain curves and maximum stress during yielding are presented in Fig. 3b and c, respectively.

Notably, the fracture process at the nanoscale occurs over a relative broad range of strain (0–40%), with the majority of stress concentration at ∼10% of strain for all glasses (Fig. 3a and b). Clear necking and the formation of molecular bridged is observed upon opening the crack (Fig. 3a), resulting in the tailing of the stress–strain curve (Fig. 3b). This characteristic is also found in other simulated glass systems, especially in the oxide and hybrid glass families.[18,32,34] The tailing is generally perceived to be a signature of the stress dissipation happening in the regions near the crack, allowing the sample at the nanoscale to dissipate energy and avoid crack opening, ultimately a form of microscopic plasticity although the glass is still macroscopically brittle. This mechanism has been found for several oxide glasses in simulations and has also been argued to have been observed in experiments.[41,42] While the shape of the stress/strain curves are largely similar for all the tested glasses, we observe decreasing maximum stress as a function of Li_2S content (Fig. 3c). This is followed by a slight widening of the main peak, especially apparent in the 60Li_2S–40SiS_2 glass (Fig. 3b), likely caused by the high modifier content creating a largely depolymerized and flexible network structure.

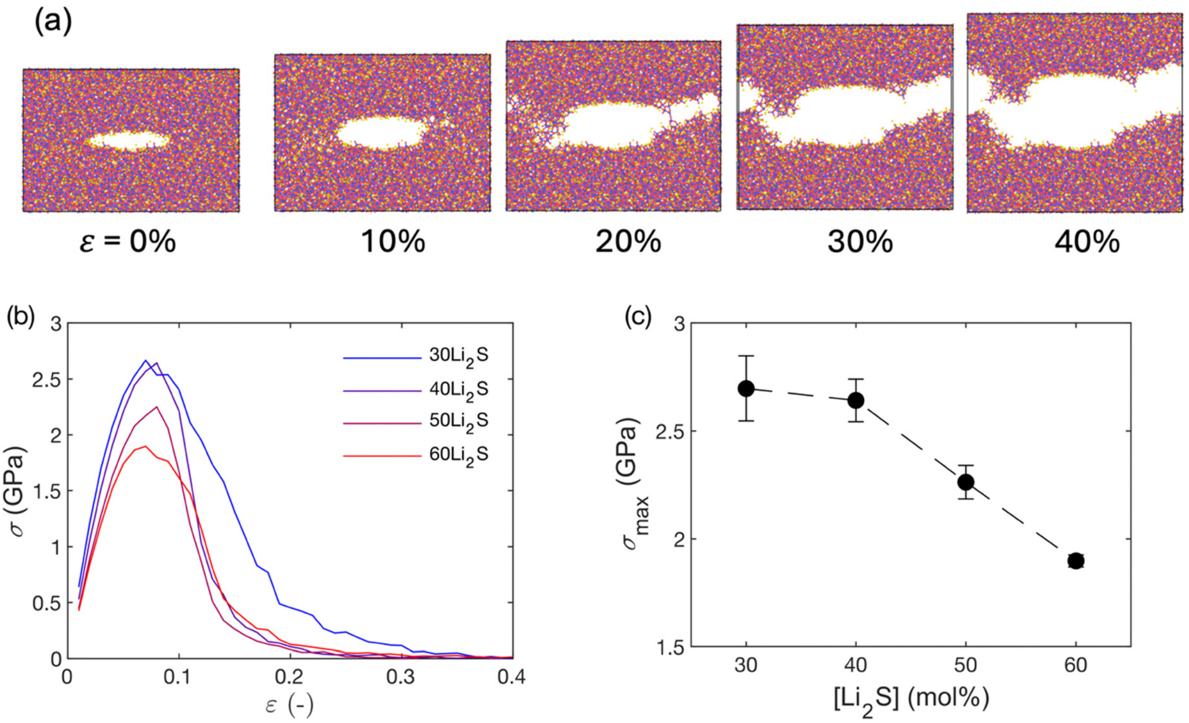

Fig. 3 (a) Atomic snapshots of the fracture process from 0% to 40% strain. (b) Averaged stress–strain curves for the four studied composition. (c) Ultimate strength as a function of Li_2S content as extracted from the fracture simulations. The dashed line in panel (c) is a guide for the eye.

The area under the stress/strain curve is proportional to the fracture energy for the opening of the crack, which in turn is correlated to the fracture toughness of the mode I crack opening (K_{Ic}, see Methods section). The estimated values of K_{Ic} are presented in Fig. 4, showing that increasing Li_2S content results in a significant decrease of K_{Ic} from $\sim$0.25 MPa $m^{0.5}$ for $30Li_2S$–$70SiS_2$ glass to $\sim$0.12 MPa $m^{0.5}$ for $60Li_2S$–$40SiS_2$ glass. In comparison, oxide glasses typically feature K_{Ic} values in the range of 0.6–0.9 MPa $m^{0.5}$.[18,43] A recent study reported a value of 0.23 MPa $m^{0.5}$ for melt-quenched Li_2S–P_2S_5 glassy electrolyte as determined from the length of indentation-induced radial cracks.[44] The herein observed decrease in K_{Ic} with increasing modifier content is a notable drawback, given how larger lithium contents are generally desired as it creates higher conductivities (as we will also show in the present study).

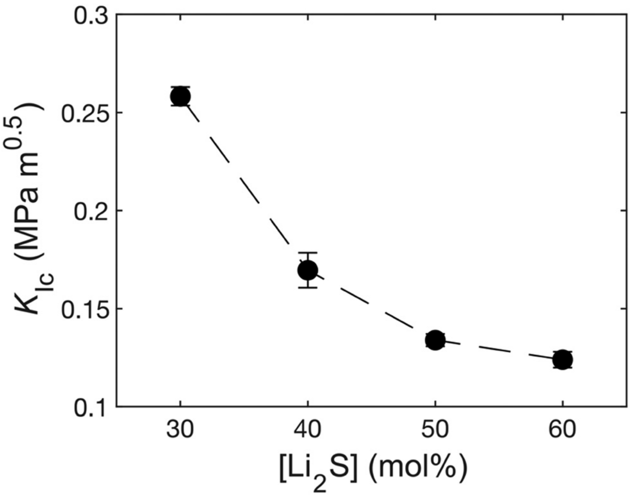

Fig. 4 Fracture toughness (K_{Ic}) as function of Li_2S content in the four studied xLi_2S–$(100-x)SiS_2$ glasses. The dashed line is a guide for the eye.

To understand the structural origin of the variation in fracture toughness, we perform a so-called bond switching analysis.[34,42,45] This involves studying the evolution of the nearest neighbors of the Si atoms as a function of the applied strain, allowing four events: (I) the coordination number remains the same with the same neighbors as a function of strain; (II) the coordination number remains the same but one or more neighbors are different compared to the initial state (swapping); (III) the coordination number increases; and (IV) the coordination number decreases. We show the bond switching results for the four glass compositions in Fig. 5. Overall, we find that the Si coordination states largely remain unchanged or swapped (Fig. 5a and b) and rarely change coordination state (Fig. 5c and d). This is meaningful as Si is mainly known to be in its 4-fold coordinated state under ambient conditions and small deformations (except for some rare cases). In addition, there is a clear trend of fewer swapping events in glasses with higher Li_2S content. This follows the observation in previous simulations of lithium borophosphate glasses[46] and may be because the larger amount of Li_2S allows for more structural rearrangement in the modifier-rich regions of the glass under the applied strain. In turn, this allows the crack to propagate

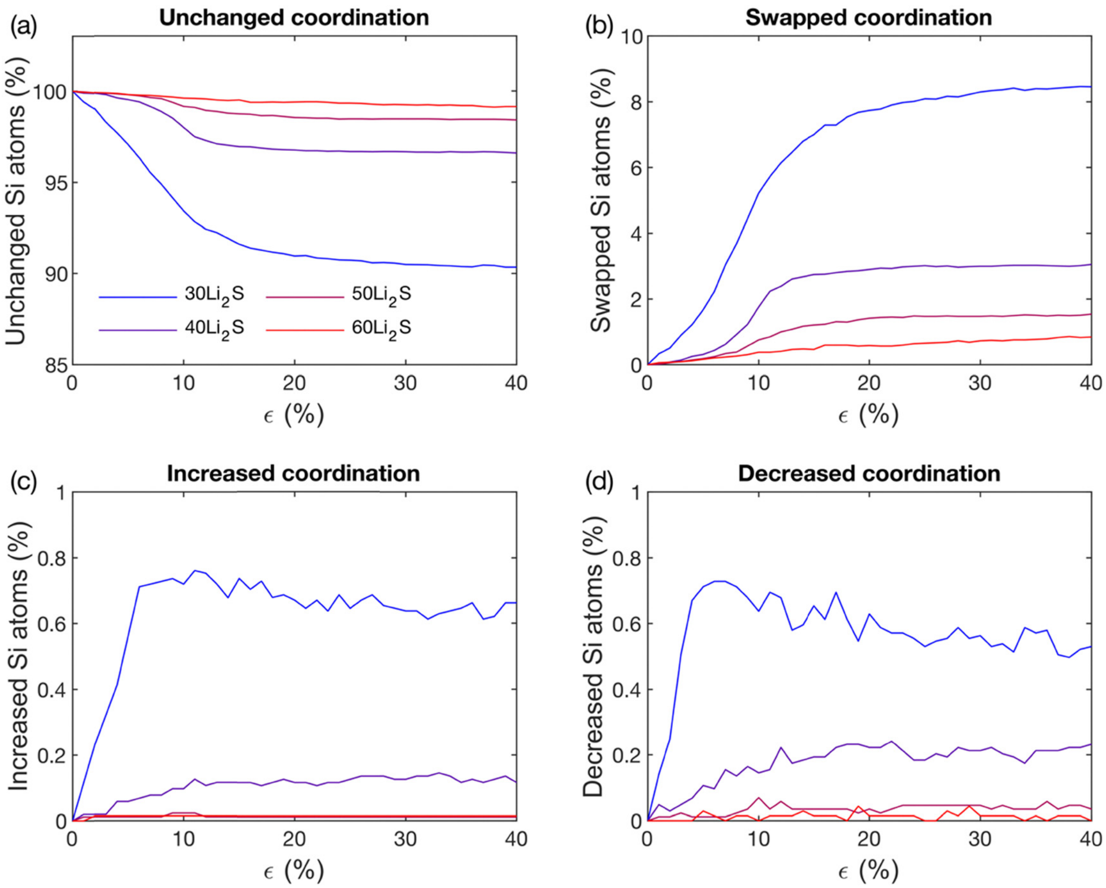

Fig. 5 Bond switching events of Si atoms as a function of applied strain in the simulated xLi$_2$S–(100−x)SiS$_2$ glasses during the forced crack opening. The silicon atoms are divided based on the coordination state as compared to the initial state. (a) Unchanged Si, *i.e.*, Si atom has exactly the same neighbors as initially. (b) Swapped Si atoms, *i.e.*, where the coordination number is the same as the initial state but at least one neighbor is different. (c) Increasing or (d) decreasing coordination number compared to the initial state.

through the modifier-rich regions (which are significantly more apparent at higher Li$_2$S content, see Fig. 1c) of the sample, thus breaking less bonds of the [SiS$_4$] tetrahedra.

We have verified that the crack passes through Li-rich regions by computing the surface mesh using the method of Krone *et al.*[47] implemented in OVITO.[35] That is, from the surface mesh, we compute the surface area of the crack opening in the glasses near the strain of crack propagation ($\varepsilon \approx 10\%$). We do so for structures consisting of all atom types and subsequently for structures where each of the different atom types (S, Si, Li) have been removed. Strikingly, we find that the computed surface area increases to the largest extent when removing Li atoms (followed by S and Si, respectively). In other words, Li atoms occupy the voids of crack growth and thus their removal leaves a void behind, effectively increasing the surface area in the vicinity of the crack. We have provided an example of this in Fig. S3 (ESI†), showcasing an 30Li$_2$S–70SiS$_2$ structure at a strain of 10% and the related surface area when removing none, all Si, all S, and all Li atoms, respectively. Here, removal of Si atoms does not result in a significant difference in surface area, while S removal slightly increases the surface area (3%). Finally, Li removal gives rise to the largest increase in surface area ($\sim$6%), indicating the initiation of cracking in the Li-rich regions of the structure.

3.3 Ionic properties

To probe the electrochemical properties of the glasses, we next compute the ionic conductivity by first calculating the mean-square displacement (MSD) of all atom types during simulations of 10 ns in a temperature range from 300 to 1600 K. As expected, we find Li to be the major charge carrier in the simulations. An example of the Li MSD from the 30Li$_2$S–70SiS$_2$ glass is shown in Fig. 6a. Mean-square displacements for the other compositions and atom types are shown in Fig. S4–S6 (ESI†). Fig. 6a shows the expected shape of the MSD, that is, at short times ($<10^2$ fs), we observe ballistic motion of atoms, followed by a plateau around MSD of 10^{-1}–10^0 Å. This is a fingerprint of the Li atoms rattling in 'cages' constituted by the polymerized Si–S network. Notably, the size of this cage is larger as the amount of Li$_2$S increases. Then, upon increasing time and temperature, we observe a transition from a ballistic to a diffusive regime as seen by the non-zero slope of the MSD when $t \rightarrow \infty$, indicating that the atoms move away from the initial 'cage' and explore other parts of the glass structure. We

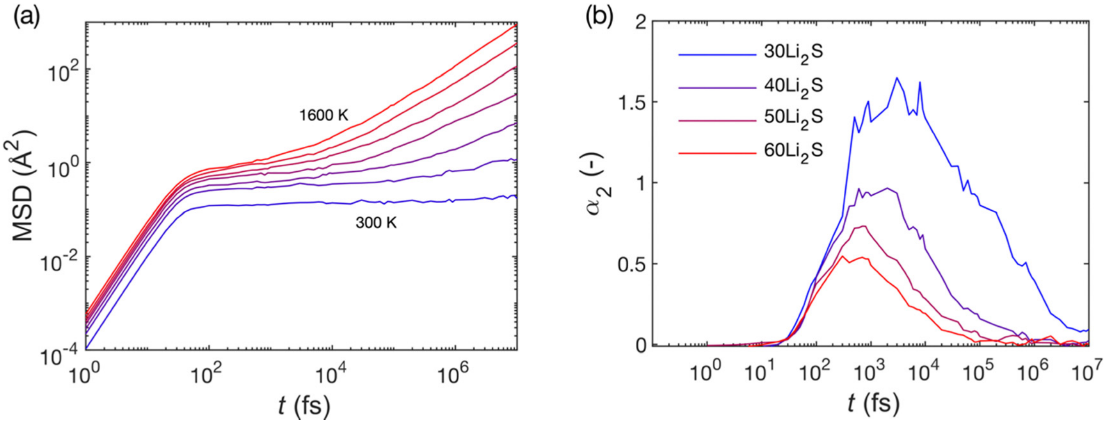

Fig. 6 (a) Mean-square displacement (MSD) of Li in the simulated 30Li$_2$S–70SiS$_2$ glass for different temperatures: 300, 600, 800, 1000, 1200, 1400, and 1600 K. (b) Non-Gaussian parameter (α_2) of Li in the simulated x = {30, 40, 50, 60} glasses in the xLi$_2$S–(100−x)SiS$_2$ series (from blue to red) over the course of a simulation time of 10 ns at a temperature of 1600 K.

find this behavior for all atom types (S, Si, Li) but the slope is significantly steeper for Li. The slope at $t \to \infty$ relates directly to the self-diffusion coefficient (D, see eqn (12) in the Methods section) of the atomic type, meaning that Li has a significantly higher D compared to Si and S for all temperatures. This confirms that Li is the main charge carrier across the studied compositional and temperature span. We have plotted the self-diffusion coefficients for all temperatures, atom types, and glass compositions in Fig. S7 (ESI†).

To further characterize the motion of the Li atoms in the systems, we calculate the so-called non-Gaussian parameter (α_2) defined as,[48]

$$\alpha_2(t) = \frac{3\langle r_{\mathrm{Li}}{}^4(t)\rangle}{5\left\langle r_{\mathrm{Li}}{}^2(t)^2\right\rangle} - 1 \tag{14}$$

where $\langle r_{\mathrm{Li}}(t)\rangle$ is the average displacement of Li atoms at a given time, t. When α_2 deviates from 0, it is a signature of non-Fickian behavior, *e.g.*, cage trapping. We present α_2 of all glasses at 1600 K in Fig. 6b (and all remaining temperatures in Fig. S8, ESI†), finding a general tendency of lower α_2 at higher temperatures and a faster approach to a diffusive regime. Comparing the four different compositions at a single temperature (Fig. 6b and Fig. S8, ESI†), we find a decrease in α_2 with increasing Li$_2$S content, *i.e.*, Li atoms in Li$_2$S-rich glasses tend to move more diffusive-like than in glasses with less Li$_2$S. This can be attributed to the decreasing network polymerization with increasing Li$_2$S content (Fig. 1c). The observed trend of α_2 is similar to that in other glass-forming electrolytic systems as well as traditional oxide glasses.[20,49,50]

Based on simulated MSDs, we calculate the diffusion coefficients as the slope of the MSD at infinite time (practically, obtainable in the state where the diffusion regime has appeared as a non-zero slope in the MSD). These diffusion coefficients are then directly linked to the conductivity of each atomic species (eqn (13)), thus allowing extraction of the total ionic conductivity of the systems at varying temperatures. We note that we do not estimate the diffusivity nor the conductivity at room temperature due to the breakdown of ergodicity at the timescales explored for the lowest temperature simulations ($<$600 K).[20] We present the conductivity of the four studied glass compositions (circles, varying color) as a function of inverse temperature and compare with experimental data[27] (squares, varying color[27]) in Fig. 7a. Generally, an expected increase of conductivity with higher temperature is found as well as an increase with the higher Li$_2$S content. This tendency is similar to that of the experimental measurements (squares in Fig. 7a).[27] However, a slight mismatch is found between extrapolations of the simulated values into the temperature range of the experiments (max T of experiments $\sim$400 K while minimum T of simulations $\sim$600 K), showing higher conductivities for the experiments. We note that we explicitly calculate the conductivity of all atom species, which is reported as the total conductivity in Fig. 7a, but practically, we find that Li is the main charge carrier and source of the calculated conductivity (see open *vs.* closed circles in Fig. 7a).

From the calculated conductivity at a range of temperatures, it is possible to extract the activation energy for conduction (E_a) through the Arrhenius relationship ($\sigma(T) \propto \exp(-E_a k_B{}^{-1} T^{-1})$). We present the activation energies for all studied glasses in Fig. 7b as well as a comparison with experimental values, finding decreasing E_a with increasing Li$_2$S contents. While there is a minor discrepancy between experiments and simulations, both feature E_a values in the same range (25–40 kJ mol^{-1}), with experimental (low temperature) values of E_a being slightly larger. This also signals a salient feature in glass-forming liquids, *i.e.*, activation barriers in low-temperature systems are systematically higher than in the liquid state. These obtained E_a values are in good agreement with those of other oxide, sulfide, and selenide-based crystalline and disordered solid-state electrolytes.[13,20,51–55] We also note that the calculated E_a for the x = 50 glass (30.5 kJ mol^{-1}) agrees well with that of another study using the same potential and composition (33.8 kJ mol^{-1}).[23] Fig. 7c shows a comparison between the experimental values of ionic conduction at room temperature and those obtained from extrapolating the

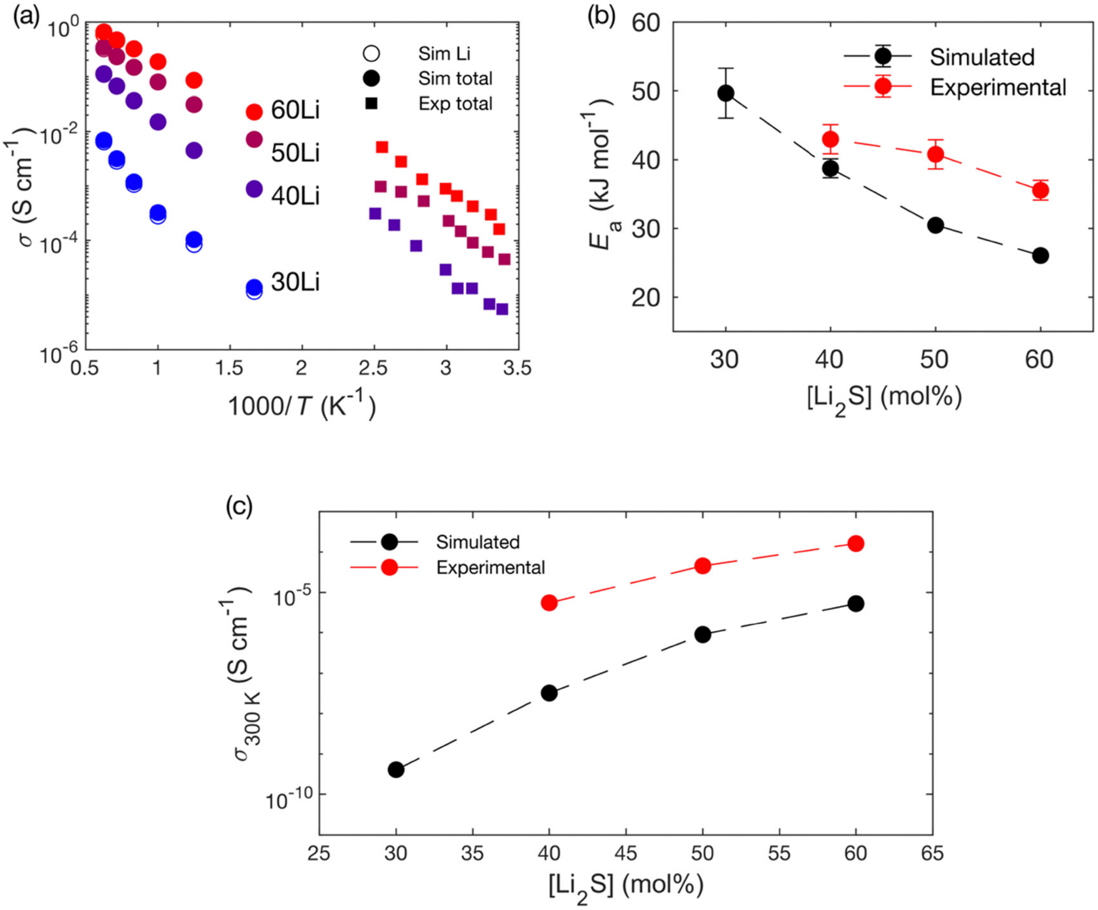

Fig. 7 (a) Ionic conductivity (σ) of the simulated x = {30, 40, 50, 60} glasses in the xLi$_2$S–(100−x)SiS$_2$ series (closed circles) and the inherent contribution from Li (open circles). Experimental conductivity data at lower temperatures are included for comparison (closed squares).[27] Note that experimental values are only given for the x = {40, 50, 60} glasses and that the values of total and Li conductivity are overlapping for nearly all values. (b) Activation energy (E_a) of the simulated (black) and experimental (red) glasses as a function of Li$_2$S content. (c) Ionic conductivity at 300 K (σ_{300K}) from experiments (red) as well as simulations (black) based on a linear extrapolation from the high-temperature data in panel (a). The dashed lines in panels (b) and (c) serve as guides for the eye.

simulation values from higher temperatures (600–1600 K) to room temperature. As described above, the simulated conductivities are generally underestimated by a factor of $\sim 10^2$. However, we observe a similar trend of increasing conductivity with increasing lithium content in both simulations and experiments. The lower conductivity in the simulations may be inherently coupled to the overestimation of the mechanical moduli given the (too) rigid networks allows for less internal adaption to moving ions – effectively better trapping Li ions in their bound cages, restricting their diffusion, and ultimately conductivity.

When comparing the mechanical and ionic properties, we interestingly find a negative proportional relation between fracture toughness and ionic conductivity ($-K_{Ic} \propto \log(\sigma)$), *i.e.*, glasses with high conductivity feature low toughness and *vice versa* (Fig. S9, ESI†). The question is whether this relation is causal, *i.e.*, if there is a relation between the dynamics of the strain- and temperature-induced dynamics. We provide a simple test of this by performing a forced stretch simulation similar to the one performed to estimate K_{Ic} (Fig. 3), but this time without a precrack to avoid possible effects of stress concentration. From this simulation, we compute the non-affine displacement (NAD), that is, the displacements of the atoms which are not directly explained by the uniaxial stretch. Fig. 8 shows the relation between the non-affine displacements after a ε = 10% strain of all Li atoms as a function of their displacement after 30 ps of simulation at 1200 K. The result is shown for the 40Li$_2$S–60SiS$_2$ glass, while results for the other compositions are presented in Fig. S9 (ESI†).

We find no clear correlation between the displacement from the temperature-induced (vertical axis of Fig. 8) and strain-induced (horizontal axis of Fig. 8) NAD, even though both displacement mechanisms are found to be enhanced by the increasing amount of Li atoms. This is likely owing to the softening of the underlying Si–S network as the extent of depolymerization increases. In turn, this points toward a decoupling of the temperature- and strain-induced displacements and thus two separate mechanisms. Despite the lack of a clear correlation, an interesting observation from Fig. 8 is that clusters of similar NAD and MSD$^{1/2}$ values appear, while other

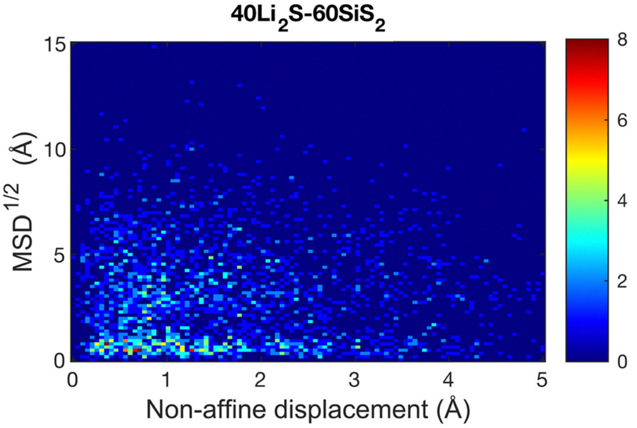

Fig. 8 Square root of mean square displacement of Li atoms (after 30 ps of simulation at 1200 K) as a function of non-affine displacement of Li atoms in a uniaxial stretching simulation (values of non-affine displacement taken after a strain of ε = 10%). All Li atoms in three independent $40Li_2S-60SiS_2$ simulations are presented. Color bar represents the number of atoms.

regions of the plot are largely depleted. This suggests that if two atoms share similar local environments, they feature similar displacement response. Interestingly, there also seems to be a band of depletion in the $MSD^{1/2}$ range of 2–3 Å (see Fig. 8 and Fig. S10, ESI†), while such depletion is not notably present in the NAD dimension. We attribute this to the temperature-induced 'hopping'' of Li ions in the Si–S backbone from their initial position to the next cage, in opposition to the smoother non-affine displacement upon stretching the cavities in which ions reside in the structure.

Ultimately, in real-life battery applications, the solid electrolyte material has the crucial role of absorbing and releasing ions, thus constantly being forced to change local dimensions in response to the local Li concentration in the material. This change of the lithium content is related to the change of Li-to-Si ratio in the studied glasses, providing insights to the *in operando* change of glass properties during battery cycling. In summary, our work highlights the challenge that while increasing Li content has a favorable impact on the ionic conductivity, it lowers the inherent mechanical stability of the material. Ultimately, this means that we cannot provide specific optimization strategies for battery design but rather our work stresses how battery material design may require a balance between ionic and mechanical properties to ensure both good electrochemical properties as well as reliability of the batteries.

4. Conclusions

We have performed an atomistic simulation study of the electrolytic, mechanical, and fracture behavior of four lithium thiosilicate ($xLi_2S-(100-x)SiS_2$) glasses with $x = \{30, 40, 50, 60\}$. A recently developed pair potential can accurately describe the structure of experimental glasses, including the decreasing degree of polymerization with increasing Li_2S content. The latter explains the decreasing mechanical moduli with increasing amount of Li_2S. Long-timescale simulations reveal Li to be the main contributor to ionic conductivity and a significant degree of caging within the relatively rigid Si–S network. Estimations of ionic conductivity are in fair agreement with experimental data, with good reproduction of compositional trends, *i.e.*, higher Li_2S content provides higher conductivity, up to $\sim 10^{-5}$ S cm^{-1} at 300 K. Fracture simulations reveal that the fracture toughness decreases with increasing Li_2S content from $\sim$0.25 MPa m$^{0.5}$ ($30Li_2S-70SiS_2$) to $\sim$0.12 MPa m$^{0.5}$ ($60Li_2S-40SiS_2$). This is ascribed to the observation that low-Li_2S glasses feature a significant amount of Si–S bond swapping, that is, S atoms swap between different Si atoms while the Si atoms retain their coordination number. Combining the results, we find a negative relation between ionic conductivity and fracture toughness, which calls for a balance between the electrolytic and mechanical properties of battery materials to ensure sufficient battery performance and reliability.

Data availability

Examples of glass structures and analysis scripts may be found online at Github at **https://github.com/soe-2912/LiSiS_study**.

Conflicts of interest

The authors declare no competing interests.

Acknowledgements

SSS and MMS acknowledge financial support from the Independent Research Fund Denmark (1127-00003). We also acknowledge computational resources provided and administered by CLAAUDIA and BioCloud at Aalborg University. MM acknowledges financial support from Fondation MAIF pour la recherche, from Chaire d'Excellence between Sorbonne Université and Universidad Autónoma de Mexico (UNAM), and repeated funding from CNRS and Sorbonne Université.

References

1 J. B. Goodenough and K. S. Park, *J. Am. Chem. Soc.*, 2013, **135**, 1167–1176.
2 T. J.-M. Armand and J.-M. Tarascon, *Nature*, 2008, **451**, 652–657.
3 J. Wen, Y. Yu and C. Chen, *Mater. Express*, 2012, **2**, 197–212.
4 T. Famprikis, P. Canepa, J. A. Dawson, M. S. Islam and C. Masquelier, *Nat. Mater.*, 2019, **18**, 1278–1291.
5 Q. Zhao, S. Stalin, C. Z. Zhao and L. A. Archer, *Nat. Rev. Mater.*, 2020, **5**, 229–252.
6 V. Viallet, V. Seznec, A. Hayashi, M. Tatsumisago and A. Pradel, *Springer Handbook of Glass*, 2019, pp. 1695–1752.
7 J. C. Bachman, S. Muy, A. Grimaud, H. H. Chang, N. Pour, S. F. Lux, O. Paschos, F. Maglia, S. Lupart, P. Lamp, L. Giordano

and Y. Shao-Horn, American Chemical Society, *ChemRev*, 2016, preprint, DOI: 10.1021/acs.chemrev.5b00563.
8 Z. A. Grady, C. J. Wilkinson, C. A. Randall and J. C. Mauro, *Front. Energy Res.*, 2020, **8**, 1–23.
9 Z. Ning, D. S. Jolly, G. Li, R. De Meyere, S. D. Pu, Y. Chen, J. Kasemchainan, J. Ihli, C. Gong, B. Liu, D. L. R. Melvin, A. Bonnin, O. Magdysyuk, P. Adamson, G. O. Hartley, C. W. Monroe, T. J. Marrow and P. G. Bruce, *Nat. Mater.*, 2021, **20**, 1121–1129.
10 N. Kim, Y. Kim, J. Sung and J. Cho, *Nat. Energy*, 2023, **8**, 921–933.
11 A. Pradel and M. Ribes, *Solid State Ionics*, 1986, **18 & 19**, 351–355.
12 M. Ribes, B. Barrau and J. L. Souquet, *J. Non-Cryst. Solids*, 1980, **38–39**, 271–276.
13 A. Pradel and A. Piarristeguy, *C. R. Geosci.*, 2022, **354**, 79–99.
14 H. Liu, Y. Liang, C. Wang, D. Li, X. Yan, C. W. Nan and L. Z. Fan, *Adv. Mater.*, 2023, **35**, 2206013.
15 *CRC handbook of Chemistry and Physics*, ed. D. R. Lide, 86th edn, CRC Press, 2005.
16 A. Kato, M. Nose, M. Yamamoto, A. Sakuda, A. Hayashi and M. Tatsumisago, *J. Ceram. Soc. Jpn.*, 2018, **126**, 719–727.
17 S. Kalnaus, A. S. Westover, M. Kornbluth, E. Herbert and N. J. Dudney, *J. Mater. Res.*, 2021, **36**, 787–796.
18 T. To, S. S. Sørensen, M. Stepniewska, A. Qiao, L. R. Jensen, M. Bauchy, Y. Yue and M. M. Smedskjaer, *Nat. Commun.*, 2020, **11**, 2593.
19 A. Dive, C. Benmore, M. Wilding, S. W. Martin, S. Beckman and S. Banerjee, *J. Phys. Chem. B*, 2018, **122**, 7597–7608.
20 S. S. Sørensen, M. M. Smedskjaer and M. Micoulaut, *J. Phys. Chem. B*, 2023, **127**, 10179–10188.
21 L.-M. Poitras and M. Micoulaut, *Phys. Rev. B*, 2023, **107**, 214205.
22 M. Micoulaut, *J. Non-Cryst. Solids*, 2024, **636**, 123017.
23 M. Micoulaut, L. M. Poitras, S. S. Sørensen, H. Flores-Ruiz and G. G. Naumis, *J. Am. Ceram. Soc.*, 2024, **107**, 7711–7726.
24 J. Christensen and J. Newman, *J. Solid State Electrochem.*, 2006, **10**, 293–319.
25 A. F. Bower, P. R. Guduru and V. A. Sethuraman, *J. Mech. Phys. Solids*, 2011, **59**, 804–828.
26 S. Kalnaus, N. J. Dudney, A. S. Westover, E. Herbert and S. Hackney, *Science*, 2023, **381**, eabg5998.
27 K. Mori, K. Iwase, Y. Oba, K. Ikeda, T. Otomo and T. Fukunaga, *Solid State Ionics*, 2020, **344**, 115141.
28 S. Nosé, *J. Chem. Phys.*, 1984, **81**, 511–519.
29 W. G. Hoover, *Phys. Rev. A: At., Mol., Opt. Phys.*, 1985, **31**, 1695.
30 D. A. Keen, *J. Appl. Crystallogr.*, 2001, **34**, 172–177.
31 L. Brochard, G. Hantal, H. Laubie, F. J. Ulm and R. J.-M. Pellenq, *Poromechanics V*, 2013, **5**, 2471–2480.
32 M. Bauchy, H. Laubie, M. J. Abdolhosseini Qomi, C. G. Hoover, F. J. Ulm and R. J. M. Pellenq, *J. Non-Cryst. Solids*, 2015, **419**, 58–64.
33 J. F. S. Christensen, S. S. Sørensen, T. To, M. Bauchy and M. M. Smedskjaer, *Phys. Rev. Mater.*, 2021, **5**, 093602.
34 T. To, S. S. Sørensen, J. F. S. Christensen, R. Christensen, L. R. Jensen, M. Bockowski, M. Bauchy and M. M. Smedskjaer, *ACS Appl. Mater. Interfaces*, 2021, **13**, 17753–17765.
35 A. Stukowski, *JOM*, 2014, **66**, 399–407.
36 R. Zhou, K. Luo, S. W. Martin and Q. An, *ACS Appl. Mater. Interfaces*, 2024, **16**, 18874–18887.
37 H. Eckert, J. H. Kennedy, A. Pradel and M. Ribes, *J. Non-Cryst. Solids*, 1989, **113**, 287–293.
38 J. E. Shelby, *Introduction to Glass Science and Technology*, The Royal Society of Chemistry, 2nd edn, 2005.
39 A. K. Varshneya, *Fundamentals of inorganic glasses*, 2013.
40 T. Rouxel, *J. Am. Ceram. Soc.*, 2007, **90**, 3019–3039.
41 F. Célarié, S. Prades, D. Bonamy, L. Ferrero, E. Bouchaud, C. Guillot and C. Marliere, *Phys. Rev. Lett.*, 2003, **90**, 75504.
42 E. J. Frankberg, J. Kalikka, F. G. Ferré, L. Joly-Pottuz, T. Salminen, J. Hintikka, M. Hokka, S. Koneti, T. Douillard, B. Le Saint, P. Kreiml, M. J. Cordill, T. Epicier, D. Stauffer, M. Vanazzi, L. Roiban, J. Akola, F. Di Fonzo, E. Levänen and K. Masenelli-Varlot, *Science*, 2019, **366**, 864–869.
43 T. Rouxel and S. Yoshida, *J. Am. Ceram. Soc.*, 2017, **100**, 4374–4396.
44 F. P. McGrogan, T. Swamy, S. R. Bishop, E. Eggleton, L. Porz, X. Chen, Y. M. Chiang and K. J. Van Vliet, *Adv. Energy Mater.*, 2017, **7**, 1602011.
45 T. To, S. S. Sørensen, Y. Yue and M. M. Smedskjaer, *Dalton Trans.*, 2021, **50**, 6126–6132.
46 Z. Chen, T. Du, S. S. Sørensen, R. Christensen, Q. Zhang, L. R. Jensen, O. V. Magdysyuk, M. Diaz-Lopez, M. Bauchy, Y. Yue and M. M. Smedskjaer, *J. Power Sources*, 2023, **553**, 232302.
47 M. Krone, J. E. Stone, T. Ertl and K. Schulten, in *Eurographics Conference on Visualization (EuroVis)*, ed. M. Meyer and T. Weinkauf, The Eurographics Association, 2012.
48 M. Vogel and S. C. Glotzer, *Phys. Rev. Lett.*, 2004, **92**, 255901.
49 J. Habasaki, K. L. Ngai and Y. Hiwatari, *Phys. Rev. E: Stat., Nonlinear, Soft Matter Phys.*, 2002, **66**, 021205.
50 J. Habasaki and K. L. Ngai, *J. Non-Cryst. Solids*, 2018, **498**, 364–371.
51 M. Tachez, J. P. Malugani, R. Mercier and G. Robert, *Solid State Ionics*, 1984, **14**, 181–185.
52 Z. Liu, W. Fu, E. A. Payzant, X. Yu, Z. Wu, N. J. Dudney, J. Kiggans, K. Hong, A. J. Rondinone and C. Liang, *J. Am. Chem. Soc.*, 2013, **135**, 975–978.
53 J. S. Thokchom and B. Kumar, *J. Power Sources*, 2008, **185**, 480–485.
54 J. Fu, *Solid State Ionics*, 1997, **104**, 191–194.
55 E. Rangasamy, J. Wolfenstine and J. Sakamoto, *Solid State Ionics*, 2012, **206**, 28–32.